Jussila, Topias; Philip, Anish; Lindén, Johan; Karppinen, Maarit

High-Quality Magnetically Hard ε-Fe_2O_3 Thin Films through Atomic Layer Deposition for Room-Temperature Applications

Published in:
Advanced Engineering Materials

DOI:
10.1002/adem.202201262

Published: 01/02/2023

Document Version
Publisher's PDF, also known as Version of record

2nd Advanced Optical Metrology Compendium

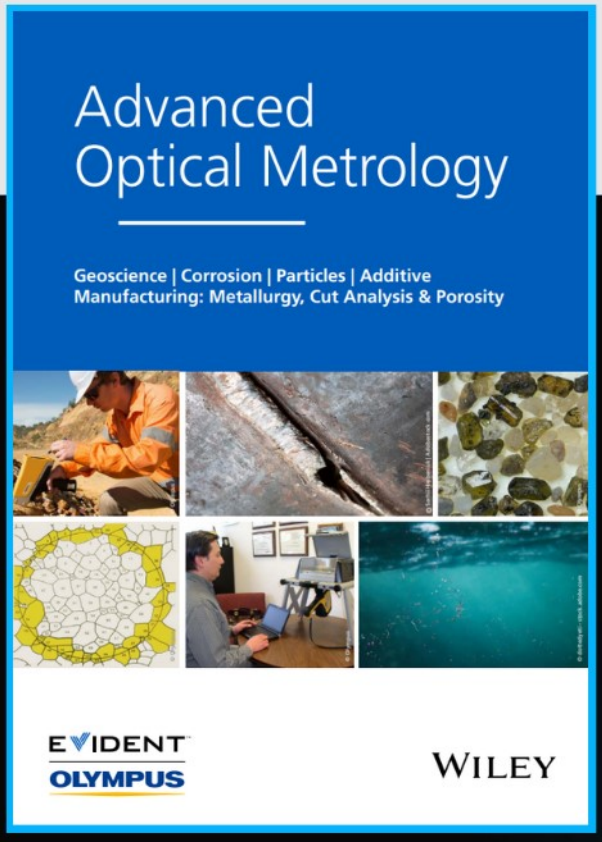

The latest eBook from Advanced Optical Metrology. Download for free.

This compendium includes a collection of optical metrology papers, a repository of teaching materials, and instructions on how to publish scientific achievements.

With the aim of improving communication between fundamental research and industrial applications in the field of optical metrology we have collected and organized existing information and made it more accessible and useful for researchers and practitioners.

EVIDENT
OLYMPUS

WILEY

ADVANCED ENGINEERING MATERIALS
www.aem-journal.com

High-Quality Magnetically Hard ε-Fe_2O_3 Thin Films through Atomic Layer Deposition for Room-Temperature Applications

Topias Jussila, Anish Philip, Johan Lindén, and Maarit Karppinen**

The critical-element-free ε-Fe_2O_3 ferrimagnet exhibits giant magnetic coercivity even at room temperature. It is thus highly attractive material for advanced applications in fields such as spintronics, high-density data storage, and wireless communication. However, a serious obstacle to overcome is the notoriously challenging synthesis of ε-Fe_2O_3 due to its metastable nature. Atomic layer deposition (ALD) is the state-of-the-art thin-film technology in microelectronics. Herein, it is demonstrated that it has also true potential for the fabrication of amazingly stable in situ crystalline and high-performance ε-Fe_2O_3 thin films from simple ($FeCl_3$ and H_2O) chemical precursors at a moderately low deposition temperature (280 °C). Standard X-ray diffraction and Fourier transfer infrared spectroscopy characterization indicates that the films are of high level of phase purity. Most importantly, precise temperature-dependent ^{57}Fe Mössbauer spectroscopy measurements verify that the hematite (α-Fe_2O_3) trace in the films is below 2.5%, and reveal the characteristic low- and high-temperature transitions at 208–228 K and ≈480 K, respectively, while magnetization measurements confirm the symmetric hysteresis loops expected for essentially phase-pure ε-Fe_2O_3 films. Excitingly, the highly *c*-axis oriented film growth, the overall film quality, and the unique magnetic properties remain the same, independently of the substrate material used.

1. Introduction

Magnetic and multiferroic thin films are attracting increasing interest owing to their high potential in next-generation spintronic applications.[1–3] However, the material repertoire suffers from complex chemical compositions and low operating temperatures.[4] Binary iron oxides would make an attractive choice owing to their simple, stable, and sustainable chemical composition based on earth-abundant, low cost, nontoxic, and biocompatible elements.[5] There are seven crystalline binary iron oxide phases, i.e., Fe_3O_4 (magnetite), α-Fe_2O_3 (hematite), γ-Fe_2O_3 (maghemite), ε-Fe_2O_3, β-Fe_2O_3, FeO (wüstite), and a recently discovered high-pressure ζ-Fe_2O_3 (zeta), of which the first four exhibit room-temperature (RT) ferrimagnetism.[6–8] Especially, the mixed-valent magnetite Fe_3O_4 is a thoroughly investigated ferrimagnet; it unfortunately suffers from tiny but influential composition variations.[9–12] The iron(III) compound ε-Fe_2O_3 possesses a giant magnetic coercivity and appreciably high Curie temperature; such magnetic characteristics are unique especially for a single-valent binary compound.[13–15] Moreover, ε-Fe_2O_3 is ferroelectric and shows high-frequency ferromagnetic resonance[16–18] and magnetoelectric coupling.[19–21] Owing to these unmatched characteristics, ε-Fe_2O_3 is considered one of the most promising materials for high-density data storage applications[18,20,22,23] and high-speed wireless communications,[16–18] among other next-generation spintronic devices.[14]

In the noncentrosymmetric orthorhombic ε-Fe_2O_3 crystal structure (space group $Pna2_1$; lattice parameters: $a = 5.095$ Å, $b = 8.789$ Å, $c = 9.437$ Å), the Fe^{3+} ions are equally distributed among four crystallographically nonequivalent iron sites including three edge-sharing octahedral sites and one corner-sharing tetrahedral site (see **Figure 1**).[15,24,25] Along the *c*-axis, the structure consists of alternating double-chained octahedral layers and single-chained octahedral layers connected by single-chained tetrahedral layers parallel to *a*-axis. Two of the octahedra (Fe_1 and Fe_2) are strongly distorted while the third octahedron (Fe_3) and the single tetrahedron (Fe_4) are regular.[26,27] The ε-Fe_2O_3 compound is isostructural with $GaFeO_3$, $AlFeO_3$, and κ-Al_2O_3.[24,25]

The high-coercivity ferrimagnetic state is seen for ε-Fe_2O_3 in the temperature range of around 110–490 K.[15,28] Above 490 K, the high-coercivity state is transformed to another ferrimagnetic state which has significantly weaker magnetic interactions;[27] the magnetic ordering is then completely lost around 850 K,

T. Jussila, A. Philip, M. Karppinen
Department of Chemistry and Materials Science
Aalto University
FI-00076 Aalto, Finland
E-mail: maarit.karppinen@aalto.fi

J. Lindén
Department of Physics
Åbo Akademi University
FI-20500 Turku, Finland
E-mail: jlinden@abo.fi

The ORCID identification number(s) for the author(s) of this article can be found under https://doi.org/10.1002/adem.202201262.

DOI: 10.1002/adem.202201262

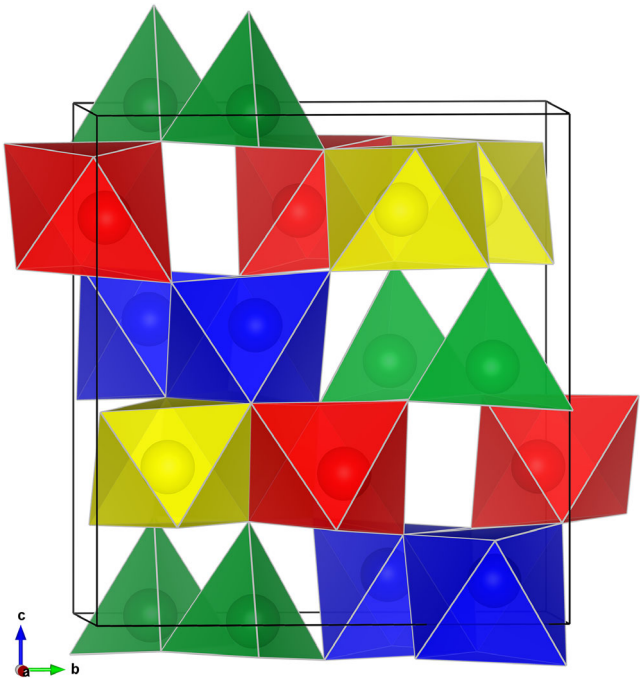

Figure 1. Polyhedral representation of the ε-Fe_2O_3 crystal structure at 300 K. The distorted octahedra are presented in blue (Fe_1) and red (Fe_2) while the regular octahedron (Fe_3) is yellow and the tetrahedron (Fe_4) is green. The crystallographic data are received from ICSD database (Coll. code 259314, García-Muñoz et al.[27]).

similar to the other iron oxides. Then, in the low-temperature range another broad magnetic transition is seen around 150–80 K,[26,28–32] resulting in an abrupt decrease in the coercivity and the so-called squareness ratio M_r/M_s (M_r = remanent magnetization, M_s = saturation magnetization) induced by structural changes and spin reorientation related phenomena.[26,28] There is still some ambiguity regarding the intriguing high-coercivity RT magnetic structure,[14] as ε-Fe_2O_3 has been proposed to behave either like a collinear ferrimagnet[25,26] or canted antiferromagnet.[15,33] In the (nearly) collinear model, initially proposed by Tronc et al.[25] and later supported by Gich et al.,[26] the net magnetization of ε-Fe_2O_3 arises from uncompensated antiferromagnetic interactions between the regular octahedral and the tetrahedral Fe sites parallel to *a*-axis. On the other hand, Kurmoo et al.[15] suggested that antiferromagnetic interactions between the tetrahedral Fe ions induce frustration of the octahedra, resulting in canted antiferromagnetic ground state.

Natural occurrence of ε-Fe_2O_3 is negligible and so far its synthesis has been limited to nanoscale quantities only due to its extremely narrow thermal stability range between the more stable γ-Fe_2O_3 and α-Fe_2O_3 polymorphs.[13,25,29] Jin et al.[13] were the first to synthesize phase pure ε-Fe_2O_3 nanoparticles in 2004; their nanoparticles fabricated by reverse–micelle and sol–gel synthesis exhibited enormous RT coercive field of 20 kOe. Later, the synthesis of high-quality ε-Fe_2O_3 nanoparticles has been demonstrated by other groups as well.[29,32,34–37]

Considering the potential applications of ε-Fe_2O_3, it is important to fabricate this unique magnetic material in high-quality thin-film form with an industrially feasible deposition technique. Gich et al.[38] pioneered the pulsed laser deposition (PLD) process of ε-Fe_2O_3 thin films in 2010. Impressively, a strong in-plane RT coercivity value of 8 kOe was measured for the films,[38] which is only slightly inferior to the highest values (≈20 kOe) reported for the ε-Fe_2O_3 nanoparticles. Corbellini et al.[39] determined the Curie temperature for their PLD-fabricated ε-Fe_2O_3 thin film at 460 K which is close to values seen for the nanoparticles (≈490 K). Ferroelectricity and magnetoelectric coupling have also been demonstrated for PLD ε-Fe_2O_3 films.[20] However, deposition of ε-Fe_2O_3 films by PLD tends to require remarkably high deposition temperatures (700–900 °C) and a lattice-matching substrate.[20,38–40]

More recently, we developed a facile atomic layer deposition (ALD) process for the growth of "XRD-pure" and highly stable ε-Fe_2O_3 thin films from $FeCl_3$ and H_2O precursors at a relatively low deposition temperature of 280 °C on "nonlattice-matching" silicon substrates.[41] Later, Tamm et al.[42] reported high coercivity value of 9.7 kOe for their similarly ALD-grown ε-Fe_2O_3 films, thus surpassing the highest coercivity value achieved for the PLD-grown ε-Fe_2O_3 films. The unique advantages of the ALD technique include the excellent film-thickness control and the unmatched coating conformality even on high-aspect ratio surfaces.[43,44] Importantly, ALD allows also growth of in situ crystalline ε-Fe_2O_3 films with preferred orientation parallel to the *c*-axis at appreciably low deposition temperatures (260–300 °C) on various substrate materials including nonlattice-matching ones. Furthermore, excitingly, it has already been demonstrated that the ALD-grown ε-Fe_2O_3 layers can be straightforwardly implemented in various multilayer structures, e.g., in combination with other ALD-grown inorganic layers (BiOCl and SiO_2) or molecular layer deposition (MLD)[45] grown organic layers (benzene or azobenzene) to achieve additional functionalities without compromising the intrinsic magnetic characteristics of the ε-Fe_2O_3 layers.[23,46–50]

Previously, ALD has also been used for the fabrication of other magnetic iron-oxide thin films, such as Fe_3O_4[51,52] and $BiFeO_3$,[53,54] but compared to ε-Fe_2O_3 these materials are notably softer ferromagnets with RT coercivity values well below 1 kOe. On the other hand, inverse-spinel structured $(Fe,Co)_3O_4$ films with similar RT coercivity values as those achieved for ε-Fe_2O_3 films have been fabricated with ALD, but only through more severe conditions, i.e., plasma-enhanced ALD plus subsequent postannealing or ozone-based ALD.[55,56] These results should be also compared to the $(Fe,Co)_3O_4$ films deposited through other techniques; for example, Shirsath et al.[57,58] fabricated $(Fe,Co)_3O_4$ films on Si/SiO_2 through DC magneto-sputtering with controlled and tunable growth orientation and extremely high perpendicular coercivity of 11.3 kOe. However, the high coercivity, induced by oxygen deficiency, was achieved only after postannealing at 800 °C.

In this work, we employ for the first time Mössbauer spectroscopy measurements to verify the high purity of the in situ crystalline ε-Fe_2O_3 thin films fabricated through our facile low-temperature ALD process. We are especially concerned about the possible traces of other iron oxide phases that are difficult to detect with other characterization techniques. Remarkably, the measurements could be realized for the relatively thin ε-Fe_2O_3 films by depositing the films on essentially gamma-ray transparent polyimide substrates and then cutting

the substrates into smaller pieces and piling them on top of each other prior to Mössbauer analysis to obtain higher total film thickness and stronger Mössbauer response. We will demonstrate that our ALD ε-Fe_2O_3 thin films are of high purity (α-Fe_2O_3 content less than 2.5%). In addition, both the low- and high-temperature magnetic transitions are discussed, and the characteristic Curie temperature (≈480 K) is confirmed for the ALD thin films. This work does not only provide unprecedented information about the ε-Fe_2O_3 thin films but also pioneers in applying Mössbauer spectroscopy as an intriguing characterization tool for iron-based ALD thin films.

2. Results and Discussion

Figure 2 summarizes the basic sample characterization results for our ALD ε-Fe_2O_3 thin-film samples, obtained from X-ray diffraction (XRD), Fourier transform infrared spectroscopy (FTIR), and magnetic measurements. All these measurements indicate toward the high phase purity of the films. All the features in the XRD pattern displayed in Figure 2a can be readily assigned to the known orthorhombic crystal structure ($Pna2_1$) of ε-Fe_2O_3;[14,23,41] the indices given are from Le Bail full profile fitting.[41] Based on the absence of the expected 113 and 200 reflections at around 35° and the 053 reflection at 60.4°, and the fact that the 002 and 004 reflections are relatively strong compared with the case of randomly oriented ε-Fe_2O_3,[41] it seems that our ε-Fe_2O_3 films show strong tendency for orientation parallel to *c*-axis. The FTIR spectrum displayed in Figure 2b shows the characteristic peaks of iron oxide at 415, 484, 560, and 675 cm^{-1},[23,46] but is free from other visible features. Especially, no indication of hydroxide or chloride traces is seen in the FTIR spectrum; these impurities could derive from the ALD precursors employed.

The morphology of the films was investigated through X-ray reflectivity (XRR) and scanning electron microscopy (SEM). Based on the XRR fitting (Figure S1, Supporting Information), the surface roughness for the 60 nm ε-Fe_2O_3 film was 2.15 nm. The grain morphology with an average grain size of ≈100 nm was found to be very similar to the cases in previous reports,[41,46] and virtually nondependent of the substrate material used (Figure S2 and S3, Supporting Information). Differences were however seen in the large-scale images depending on the substrate material, as the film surface was smooth on silicon but exhibited longitudinal bulge patterns on Kapton (Figure S3, Supporting Information). This might be due to poorer adhesion on Kapton with less active surface sites,[59] causing also some cracking of the growing film at the bulges (Figure S4, Supporting Information). It should be noted that in previous works the adhesion issue of Kapton has been tackled using a plasma treatment or by depositing a thin Fe–organic interface layer.[50,59]

The strong ferrimagnetic behavior of the ε-Fe_2O_3 film deposited on Kapton is revealed from Figure 2c. Both the in-plane coercivity and the high-field magnetization increase, from 1.2 to 4.9 kOe and 7.8×10^{-3} to 8.6×10^{-3} emu (at 50 kOe), respectively, when the temperature is decreased from 400 to 10 K.

The RT in-plane coercivity value of 2 kOe seen for the present films is reasonable for polycrystalline (partly oriented) thin films and very similar to the values reported for epitaxial ε-Fe_2O_3 films deposited via PLD.[20,40] The in-plane coercivity is ≈25% higher compared to the out-of-plane coercivity (≈1.6 kOe) of ALD-grown ε-Fe_2O_3 measured in our previous work. This is reasonable considering the preferred growth orientation being parallel to the *c*-axis (magnetic hard axis), denoting that the magnetic easy axis of ε-Fe_2O_3 (*a*-axis) is parallel (in-plane) to the film surface.

It is important to note that the magnetic properties of our ALD ε-Fe_2O_3 films are essentially nondependent of the substrate (Si or Kapton) employed, which demonstrates the possibility to deposit ε-Fe_2O_3 thin films on a wide spectrum of material surfaces through ALD as no lattice-matching substrates are required.[23] Furthermore, all the hysteresis loops shown in Figure 2c are perfectly symmetric; this emphasizes the high quality of the films. For example, for PLD-grown ε-Fe_2O_3 films asymmetric hysteresis loops with an additional magnetization step (necking) are typically seen, most likely resulting from magnetically softer γ-Fe_2O_3 and/or Fe_3O_4 impurity phases.[38,39]

The Mössbauer spectra recorded at 208, 228, 305, and 433 K are shown in **Figure 3**a. As could be expected for ε-Fe_2O_3,[25,26] the spectra are well described by three high-field sextets with internal fields ranging from 34 to 44 T and one low-field component with an internal field less than 30 T (Figure 3b), as well as

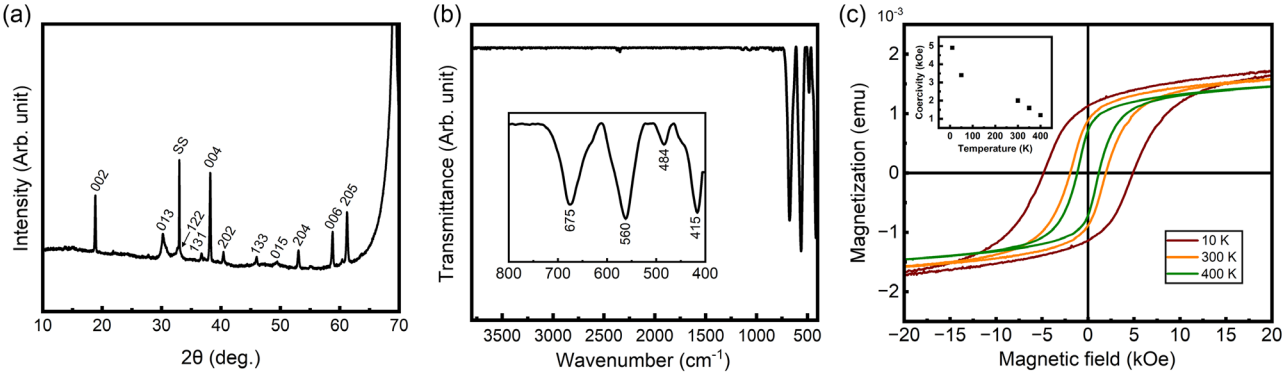

Figure 2. Basic characterization results for 204 nm-thick ε-Fe_2O_3 films (grown in a and b on silicon, and in c on Kapton): a) XRD pattern, in which the Miller indices are for the orthorhombic ($Pna2_1$) ε-Fe_2O_3 structure, while the peak caused by the Si substrate is marked with SS. b) FTIR spectrum after subtraction of the substrate contribution. c) *M–H* curves measured at 10, 300, and 400 K; the inset shows the temperature dependence of magnetic coercivity.

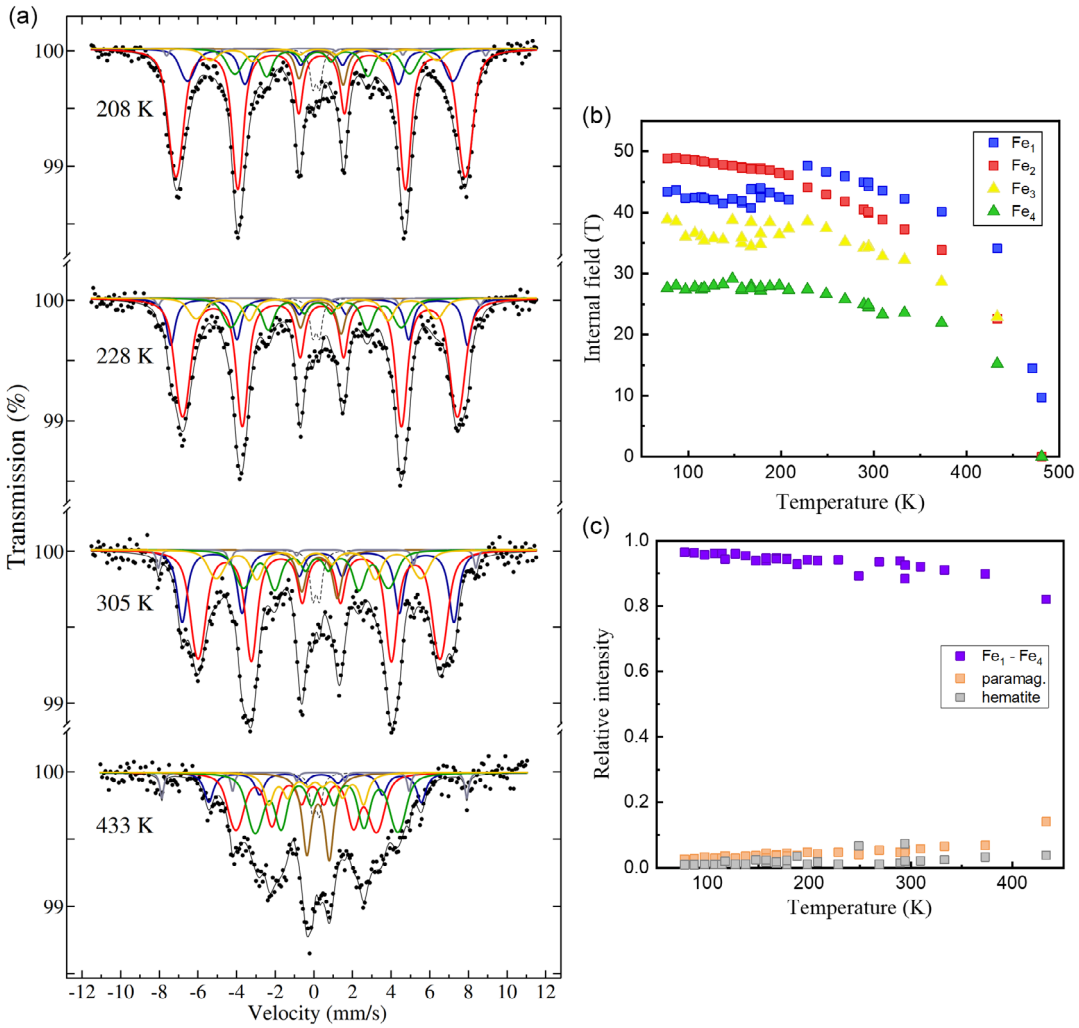

Figure 3. a) Mössbauer spectra recorded for ε-Fe_2O_3 at indicated temperatures. The sextets reflecting iron at the four sites are drawn in red, blue, green, and yellow. The sextet due to hematite impurity is gray and the paramagnetic doublet is drawn in brown. Traces due to Fe impurities in the Be window of the detector are drawn with a black dashed line. The two topmost spectra are recorded on either side of the low-temperature transition. b) Internal fields of the four ε-Fe_2O_3 components. c) Relative intensities of the four iron components combined (violet), and the paramagnetic (orange) and hematite (gray) components as function of temperature.

one paramagnetic doublet with a negative quadrupole coupling constant. The isomer shift values (0.2–0.4 mm s^{-1} at RT) are typical for high-spin trivalent iron. As explained later on, these five components covering ≈98% at RT of the total intensity are believed to originate from the ε-Fe_2O_3 phase. Besides these components, the tiny sextet covering only ≈2.5% of the intensity could be seen and assigned to α-Fe_2O_3 (hematite) due to its 51.5 T field and narrow linewidth. This component was barely visible in the low-temperature spectra but became little better visible as the temperature was increased, as it retained its high internal-field value up to 481 K (the highest measurement temperature in this study). Figure 3c shows the temperature dependence of the relative intensities of the magnetically hard ε-Fe_2O_3 phase (the four distinct iron sites combined), and both the paramagnetic and hematite components. Most importantly, the low intensity of the hematite impurity component verifies the high phase purity of our ε-Fe_2O_3 thin film.

Based on the XRD data (Figure 2a), the present thin films exhibited signatures of orientation. This orientation can be seen as lower-than-expected intensities for the outer lines (lines 1 and 6) of the sextets in the Mössbauer spectra; for randomly oriented samples, the intensities of the spectral lines should decrease going from the outermost lines to the inner lines but in Figure 3a the outermost lines have lower intensity compared to the lines 2 and 5. The fitted values were close to 63° at all temperatures, where the so-called magic angle value 54.73° is obtained for a sample of random orientation of the local quantization axes. In epitaxial films, it is not unusual to have $\theta = 90°$.

As for the detailed assignments of the different components originating from the ε-Fe_2O_3 phase, based on previous reports for ε-Fe_2O_3 nanoparticle samples, two of the components with the highest internal field could be tentatively assigned for the two distorted octahedral Fe^{3+} sites of ε-Fe_2O_3 (Fe_1 and Fe_2), while the third component could be due to the regular octahedral

site (Fe_3) and the low-field component would most probably originate from the tetrahedral site (Fe_4).[26,29] It is noteworthy that the relative intensities of these components differ from the theoretical 25% each as the intensity of the tetrahedral site is ≈19% (at RT) of the total intensity of the four iron components. As ALD films are grown in a layer-by-layer manner, there can be a higher tendency for certain crystallographic planes to induce the formation of grain boundaries easier than other planes.[60] As a result, the relative number of the different crystallographic sites of the whole material would change. Hence, tentatively, the cause for the different relative site occupancies in the ε-Fe_2O_3 thin films could be a higher tendency of grain formation prior to the tetrahedral sites, thus resulting in lower total Fe_4 intensity.

The paramagnetic component seen in the spectra throughout the whole temperature range most likely originates from a minute amount of small (≈5 nm) ε-Fe_2O_3 superparamagnetic crystallites.[15,30] As the temperature increases, the relative intensity of this paramagnetic component slowly increases, as larger and larger crystallites gradually become (super)paramagnetic. Verification of the crystal phase of the superparamagnetic particles would require Mössbauer analysis with liquid helium at ≈5 K to reach the blocking temperature and, thus, to distinguish the four sextets of ε-Fe_2O_3 without the paramagnetic component.[30] We tentatively suggest that the superparamagnetic particles can be more abundant near the substrate–film interface due to the porous nature of the polymer substrate which can induce growth of small iron oxide clusters inside the pores of uppermost layers of the substrate as the small ALD precursors are diffused into the substrate during the initial stage of the deposition process.[61] Consequently, the concentration of the small paramagnetic crystallites could be expected to be smaller on a dense, inorganic substrates (such as silicon). Nevertheless, even in the present films grown on Kapton for the Mössbauer characterization, the intensity of the paramagnetic component is appreciably low, and—importantly—low enough not to affect the magnetic hysteresis characteristics of the films (Figure 2c).

Owing to the orientation, the negative sign of the quadrupole coupling constant for the paramagnetic doublet could be established. The relative intensity of the doublet increased slowly with temperature and more quickly when the magnetic transition temperature (T_C) of ≈480 K was approached. At 481 K (**Figure 4**), the obtained Mössbauer spectrum was practically paramagnetic. No indication of a high-temperature magnetic phase was observed, although the spectrum in Figure 4 still exhibits weak magnetic "wings" on either side of the doublet. The magnetic transition temperature can be also deduced from Figure 3b; at 481 K, only one (Fe_1) of the four components exhibits a weak internal field, indicating that the magnetic transition of the ε-Fe_2O_3 phase occurs in this temperature range. Most likely, if the temperature would be increased slightly higher, the internal field of the last component would also go to zero.

The almost completely paramagnetic spectrum recorded at 481 K was fitted using two quadrupole doublets differing only slightly in isomer shift values and quadrupole splitting. However, lingering weak magnetism may have caused some broadening of the spectrum, making the assignment of the components uncertain. Regardless, the intensity ratio of the doublets is close to 3:1, matching with the 3:1 ratio of the three octahedral and one tetrahedral sites of ε-Fe_2O_3. Slight differences in the quadrupole doublets are expected due to the different oxygen coordination.

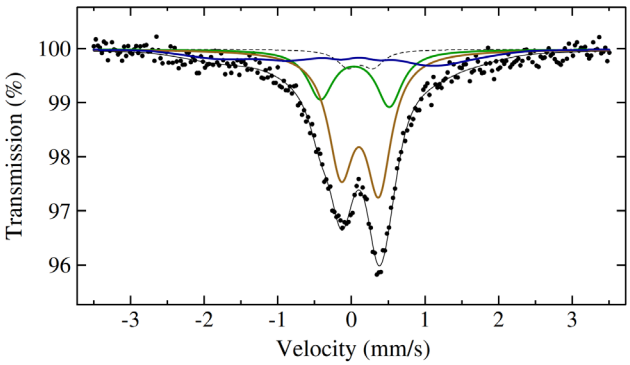

Figure 4. Spectrum recorded from the ε-Fe_2O_3 sample at 481 K. The navy blue component is due to small amount of magnetically ordered Fe, while the paramagnetic feature was fitted using two asymmetric doublets (brown and green). Traces due to Fe impurities in the Be window of the detector are drawn with a black dashed line.

At 77 K the spectrum is dominated by one 49 T component, almost overshadowing the hematite impurity. The three other ε-Fe_2O_3 components are still visible, but with much lower intensities. The two other high-field components have increased their field to 39 and 44 T, respectively, while the low-field has $B = 28$ T. Upon increasing temperature the fields slowly decrease, following a Brillouin-like behavior, and the dominating component loses intensity to the three other components, but the evolution was initially more gradual than reported for the nanoparticles, where the transition occurs between 110 and 150 K.[26] However, between 208 and 228 K, a discontinuity occurs for the internal fields (Figure 3b) of the high-field component which is increased by 1–2 T, rather similarly to nanoparticles at 110–150 K. The discontinuity is not observed for the isomer shift values. The shifted temperature change of the low-temperature transition might be caused by the strain effects induced by the substrate.[62,63]

Interestingly, the tetrahedral iron (Fe_4) does not experience any discontinuity around the low-temperature transition, in clear contrast to the behavior seen in nanoparticles.[15,26,33] When approaching the transition from the higher temperature side, the internal field of Fe_4 of ε-Fe_2O_3 nanoparticles increased significantly (≈20%) which was assigned to an increased distortion of the tetrahedral site.[26] This was also thought to be the reason for the abrupt weakening of magnetization seen for the nanoparticle samples because the net magnetization arising from antiferromagnetic interactions between Fe_3 and Fe_4 is notably reduced as a result of the increased field of Fe_4.[26,31] For our ALD grown ε-Fe_2O_3 thin films, on the other hand, the strong weakening of the magnetization is not observed,[41] being in accordance with the continuous Fe_4 field.

The reason for the different behavior of Fe_4 remains unclear. Contributing factors could be the grain boundaries and the deviation of the theoretical iron occupancies in the structure and, relatedly, different degrees of distortion of the polyhedra. This could also explain why the internal values of the four iron components in general were slightly lower and why the distorted Fe_1 and Fe_2 were more distinguishable (larger difference in internal

fields) from each other in the thin film as compared to the bulk-type structure.

3. Conclusions

In this study, ^{57}Fe Mössbauer measurements were successfully applied for studying the phase purity, magnetic transitions, and hyperfine interactions of ε-Fe_2O_3 thin film deposited on Kapton tape through ALD. The hematite impurity covered only 2.5% of the spectral intensity, confirming the high phase purity of our ALD-grown ε-Fe_2O_3 films. In addition, a minute paramagnetic component most likely originating from small superparamagnetic iron oxide particles was observed. Overall, the ε-Fe_2O_3 films were of high purity, which was also seen from the symmetric magnetic hysteresis loops, free from the necking caused by softer magnetic impurity phases.

Four spectral components originating from the four crystal sites in ε-Fe_2O_3 were discerned in the Mössbauer spectra. The theoretical 25% each component intensity for the magnetically ordered sextets was approached with increasing temperature but not completely reached until hitting the Curie temperature around 481 K. As compared to reported bulk (nanoparticle) material, the low-temperature transition occurring between 110 and 150 K was shifted to a higher temperature range, between 208 and 228 K, but distinctly seen from the Mössbauer data. The non-ideal site intensities and the shifted transition temperature were tentatively assigned to grain boundaries and strain induced by the substrate.

The high Curie temperature was also confirmed for the films; the spectrum obtained at 481 K was practically paramagnetic with weak magnetic wing features of the ongoing demise of the magnetic order. No indication of a high-temperature magnetic phase was observed for this thin-film sample. The implementation of the Mössbauer spectroscopy for ε-Fe_2O_3 thin films allowed precise investigation of the composition and magnetic characteristics, hence proving the applicability and high value of Mössbauer spectroscopy for ALD thin films.

4. Experimental Section

The ε-Fe_2O_3 films were deposited at 280 °C in a flow-type hot-wall ALD reactor (F-120 by ASM Ltd.). Iron chloride (Merck, 95%) and deionized water were used as precursors. The $FeCl_3$ powder was placed inside the reactor in an open boat and heated to 158 °C for evaporation, whereas the deionized water was kept in a cylinder outside the reactor at RT. Reactor pressure was kept at 3–5 mbar; nitrogen (99.999%, flow rate 300 SCCM) was used both as carrier gas and purging gas. Parallel depositions were carried out on 3×3 cm^2 silicon wafers (with a native oxide layer) for basic characterization, and on 4×4 cm^2 Kapton (polyimide) tape for both magnetic and Mössbauer measurements. The number of ALD cycles applied was fixed to 4000 for samples intended for Mössbauer and SEM characterizations, to yield 204 nm-thick in situ crystalline ε-Fe_2O_3 coatings as confirmed with spectroscopic ellipsometry and XRD.

The spectroscopic ellipsometry measurements (J.A. Woollam M-2000UI; 240–1700 nm) were carried out for films deposited on silicon substrates. The data were fitted with the CompleteEASE software. Crystal structure of the films was verified with XRD (X'Pert MPD PRO Alfa 1, PANalytical; Cu $K\alpha_1$ radiation). Additionally, an XRR measurement was carried out for a 60 nm ε-Fe_2O_3 film with the same equipment. The XRR curve was fitted with X'Pert Reflectivity software (PANalytical) to obtain estimates for the film density and roughness. FTIR spectroscopy (Bruker alpha II) was used to investigate the chemical bonding in the films; the contribution of silicon substrate was subtracted from the measured FTIR spectra. The film morphology was investigated for ε-Fe_2O_3 films deposited on both silicon and Kapton substrates with SEM (Tescan Mira 3) imaging. The specimens were mounted on specific sample holders by applying a conductive carbon tape and, prior to the imaging, the films were coated with a ≈5 nm-thick conductive coating through sputtering (Quorum Q150T ES Sample Coater) using an Au/Pd 80/20 target.

Magnetic properties were studied using a vibrating sample magnetometer (VSM; Quantum Design PPMS). The measurement was done for a ε-Fe_2O_3 film grown on 3×4 mm^2 Kapton substrate; this sample was glued with GE varnish on a quartz plate. The magnetic field was applied parallel to the film surface (in-plane direction) between −50 and 50 kOe.

The ^{57}Fe Mössbauer measurements were performed in transmission geometry using a 2 year old 50 mCi Co-57(Rh) source from Rietverc Co. A linear Doppler velocity with maximum velocities of 11–11.5 mm s^{-1} was used. The absorber was made by cutting the films deposited on Kapton tape in circular pieces with a diameter of 18 mm and stapling them on top of each other to get a stack of 16 layers (total iron oxide thickness ≈3.26 μm). The absorber was measured at temperatures between 77 and 305 K, using an Oxford ITC-506 continuous-flow cryostat equipped with an ITC4 temperature controller. At temperatures between 333 and 481 K, a home-built resistive furnace was used to heat the sample. The temperature was controlled using a Keithley 9700 temperature controller and the furnace was continuously flushed with a small flux of dry N_2 gas to prevent oxidation.

The spectra obtained were fitted using five magnetically split sextets with the internal field, quadrupole coupling constant, isomer shift, and relative component intensity as fit parameters. Due to sample texturizing (orientation of the film), the angle (θ) between the direction of the gamma quanta and the local quantization axis (direction of the internal field) was also fitted. One global θ parameter was used for all components. Additionally, a paramagnetic doublet, with the quadrupole coupling constant, isomer shift, and relative component intensity as fit parameters, was used. All components were constrained to have equal linewidth Γ, except a sextet assigned to α-Fe_2O_3 which had clearly narrower linewidth.

Additional broadening of the sextets was handled using a Gaussian distribution of the internal field with the width of the distribution (ΔB) as a fit parameter. Traces of iron in the beryllium window of the detector and the heat shields of the furnace were modeled using a small quadrupole doublet with fixed split and isomer shift.

Supporting Information

Supporting Information is available from the Wiley Online Library or from the author.

Acknowledgements

The authors acknowledge the funding from Academy of Finland (PREIN Flagship), and the use of the RawMatTERS Finland Infrastructure (RAMI) at Aalto University.

Conflict of Interest

The authors declare no conflict of interest.

Data Availability Statement

The data that support the findings of this study are available from the corresponding author upon reasonable request.

Keywords

ε-Fe_2O_3, ALD, atomic layer deposition, magnetic thin films, Mössbauer spectroscopy, thin films

Received: September 1, 2022
Revised: October 15, 2022
Published online: November 17, 2022

[1] M. S. Ansari, M. H. D. Othman, M. O. Ansari, S. Ansari, H. Abdullah, *Appl. Mater. Today* **2021**, *25*, 101181.
[2] T. Amrillah, C. A. C. Abdullah, D. P. Sari, Z. Mumtazah, F. P. Adila, F. Astuti, *Cryst. Growth Des.* **2021**, *21*, 7326.
[3] L. Guo, X. Gu, X. Zhu, X. Sun, *Adv. Mater.* **2019**, *31*, 1805355.
[4] J. F. Scott, *NPG Asia Mater.* **2013**, *5*, e72.
[5] L. Machala, J. Tuček, R. Zbořil, *Chem. Mater.* **2011**, *23*, 3255.
[6] R. Zboril, M. Mashlan, D. Petridis, *Chem. Mater.* **2002**, *14*, 969.
[7] J. Tuček, L. Machala, S. Ono, A. Namai, M. Yoshikiyo, K. Imoto, H. Tokoro, S.-I. Ohkoshi, R. Zbořil, *Sci. Rep.* **2015**, *5*, 15091.
[8] R. M. Hazen, R. Jeanloz, *Rev. Geophys.* **1984**, *22*, 37.
[9] E. J. W. Verwey, *Nature* **1939**, *144*, 327.
[10] E. Lochner, K. A. Shaw, R. C. DiBari, W. Portwine, P. Stoyonov, S. D. Berry, D. M. Lind, *IEEE Trans. Magn.* **1994**, *30*, 4912.
[11] F. Walz, *J. Phys.: Condens. Matter* **2002**, *14*, R285.
[12] J. Mazo-Zuluaga, J. Restrepo, J. Mejía-López, *J. Phys.: Condens. Matter* **2008**, *20*, 195213.
[13] J. Jin, S. Ohkoshi, K. Hashimoto, *Adv. Mater.* **2004**, *16*, 48.
[14] J. Tuček, R. Zbořil, A. Namai, S.-I. Ohkoshi, *Chem. Mater.* **2010**, *22*, 6483.
[15] M. Kurmoo, J.-L. Rehspringer, A. Hutlova, C. D'Orléans, S. Vilminot, C. Estournès, D. Niznansky, *Chem. Mater.* **2005**, *17*, 1106.
[16] H. Tokoro, K. Nakabayashi, S. Nagashima, Q. Song, M. Yoshikiyo, S.-I. Ohkoshi, *Bull. Chem. Soc. Jpn.* **2022**, *95*, 538.
[17] S. Ohkoshi, S. Kuroki, S. Sakurai, K. Matsumoto, K. Sato, S. Sasaki, *Angew. Chem., Int. Ed. Engl.* **2007**, *46*, 8392.
[18] A. Namai, M. Yoshikiyo, K. Yamada, S. Sakurai, T. Goto, T. Yoshida, T. Miyazaki, M. Nakajima, T. Suemoto, H. Tokoro, S.-I. Ohkoshi, *Nat. Commun.* **2012**, *3*, 1035.
[19] M. Gich, C. Frontera, A. Roig, J. Fontcuberta, E. Molins, N. Bellido, C. Simon, C. Fleta, *Nanotechnology* **2006**, *17*, 687.
[20] M. Gich, I. Fina, A. Morelli, F. Sánchez, M. Alexe, J. Gàzquez, J. Fontcuberta, A. Roig, *Adv. Mater.* **2014**, *26*, 4645.
[21] T. Katayama, S. Yasui, Y. Hamasaki, T. Shiraishi, A. Akama, T. Kiguchi, M. Itoh, *Adv. Funct. Mater.* **2018**, *28*, 1704789.
[22] S.-I. Ohkoshi, A. Namai, M. Yoshikiyo, K. Imoto, K. Tamazaki, K. Matsuno, O. Inoue, T. Ide, K. Masada, M. Goto, T. Goto, T. Yoshida, T. Miyazaki, *Angew. Chem., Int. Ed.* **2016**, *55*, 11403.
[23] A. Philip, Y. Zhou, G. C. Tewari, S. van Dijken, M. Karppinen, *J. Mater. Chem. C* **2022**, *10*, 294.
[24] K. Kelm, W. Mader, *Z. Anorg. Allg. Chem.* **2005**, *631*, 2383.
[25] E. Tronc, C. Chanéac, J. P. Jolivet, *J. Solid State Chem.* **1998**, *139*, 93.
[26] M. Gich, C. Frontera, A. Roig, E. Taboada, E. Molins, H. R. Rechenberg, J. D. Ardisson, W. A. A. Macedo, C. Ritter, V. Hardy, J. Sort, V. Skumryev, J. Nogués, *Chem. Mater.* **2006**, *18*, 3889.
[27] J. L. García-Muñoz, A. Romaguera, F. Fauth, J. Nogués, M. Gich, *Chem. Mater.* **2017**, *29*, 9705.
[28] S. Sakurai, J. Jin, K. Hashimoto, S.-I. Ohkoshi, *J. Phys. Soc. Jpn.* **2005**, *74*, 1946.
[29] I. Khan, S. Morishita, R. Higashinaka, T. D. Matsuda, Y. Aoki, E. Kuzmann, Z. Homonnay, S. Katalin, L. Pavić, S. Kubuki, *J. Magn. Magn. Mater.* **2021**, *538*, 168264.
[30] A. A. Dubrovskiy, D. A. Balaev, K. A. Shaykhutdinov, O. A. Bayukov, O. N. Pletnev, S. S. Yakushkin, G. A. Bukhtiyarova, O. N. Martyanov, *J. Appl. Phys.* **2015**, *118*, 213901.
[31] M. Gich, A. Roig, C. Frontera, E. Molins, J. Sort, M. Popovici, G. Chouteau, D. Martín y Marero, J. Nogués, *J. Appl. Phys.* **2005**, *98*, 044307.
[32] Y.-C. Tseng, N. Souza-Neto, D. Haskel, M. Gich, C. Frontera, A. Roig, M. van Veenendaal, J. Nogues, *Phys. Rev. B* **2009**, *79*, 094404.
[33] J. L. Rehspringer, S. Vilminot, D. Niznansky, K. Zaveta, C. Estournes, M. Kurmoo, *Hyperfine Interact.* **2005**, *166*, 475.
[34] K. Mori, Y. Oaki, M. Suda, Y. Einaga, H. Imai, *Chem. Lett.* **2008**, *37*, 814.
[35] A. I. Sharapaev, S. A. Kuznetsova, A. N. Norenko, A. G. Muradova, N. P. Simonenko, E. V. Yurtov, *Russ. J. Inorg. Chem.* **2021**, *66*, 740.
[36] P. Brázda, J. Kohout, P. Bezdička, T. Kmječ, *Cryst. Growth Des.* **2014**, *14*, 1039.
[37] M. Tadic, I. Milosevic, S. Kralj, M. Mitric, D. Makovec, M.-L. Saboungi, L. Motte, *Nanoscale* **2017**, *9*, 10579.
[38] M. Gich, J. Gazquez, A. Roig, A. Crespi, J. Fontcuberta, J. C. Idrobo, S. J. Pennycook, M. Varela, V. Skumryev, M. Varela, *Appl. Phys. Lett.* **2010**, *96*, 112508.
[39] L. Corbellini, C. Lacroix, C. Harnagea, A. Korinek, G. A. Botton, D. Ménard, A. Pignolet, *Sci. Rep.* **2017**, *7*, 3712.
[40] T. M. N. Thai, D. T. Nguyen, N.-S. Lee, J.-S. Rhyee, J. Song, H.-J. Kim, *J. Appl. Phys.* **2016**, *120*, 185304.
[41] A. Tanskanen, O. Mustonen, M. Karppinen, *APL Mater.* **2017**, *5*, 056104.
[42] A. Tamm, A. Tarre, J. Kozlova, M. Rähn, T. Jõgiaas, T. Kahro, J. Link, R. Stern, *RSC Adv.* **2021**, *11*, 7521.
[43] M. Leskelä, M. Ritala, *Angew. Chem., Int. Ed.* **2003**, *42*, 5548.
[44] V. Cremers, R. L. Puurunen, J. Dendooven, *Appl. Phys. Rev.* **2019**, *6*, 021302.
[45] J. Multia, M. Karppinen, *Adv. Mater. Interfaces* **2022**, *9*, 2200210.
[46] A. Philip, J.-P. Niemelä, G. C. Tewari, B. Putz, T. E. J. Edwards, M. Itoh, I. Utke, M. Karppinen, *ACS Appl. Mater. Interfaces* **2020**, *12*, 21912.
[47] H. Seemen, K. Kukli, T. Jõgiaas, P. Ritslaid, J. Link, R. Stern, S. Dueñas, H. Castán, A. Tamm, *J. Alloys Compd.* **2020**, *846*, 156099.
[48] K. Kukli, M. Kemell, H. Castán, S. Dueñas, J. Link, R. Stern, M. J. Heikkilä, T. Jõgiaas, J. Kozlova, M. Rähn, K. Mizohata, M. Ritala, M. Leskelä, *J. Vac. Sci. Technol., A* **2020**, *38*, 042405.
[49] A. Tanskanen, M. Karppinen, *Phys. Status Solidi RRL* **2018**, *12*, 1800390.
[50] J.-P. Niemelä, A. Philip, N. Rohbeck, M. Karppinen, J. Michler, I. Utke, *ACS Appl. Nano Mater.* **2021**, *4*, 1692.
[51] R. Zierold, C. Lam, J. Dendooven, J. Gooth, T. Böhnert, P. Sergelius, F. Munnik, J. Moreno, D. Görlitz, C. Detavernier, K. Nielsch, *J. Phys. D: Appl. Phys.* **2014**, *47*, 485001.
[52] Y. Zhang, M. Liu, Y. Zhang, X. Chen, W. Ren, Z.-G. Ye, *J. Appl. Phys.* **2015**, *117*, 17C743.
[53] P. Jalkanen, V. Tuboltsev, B. Marchand, A. Savin, M. Puttaswamy, M. Vehkamäki, K. Mizohata, M. Kemell, T. Hatanpää, V. Rogozin, J. Räisänen, M. Ritala, M. Leskelä, *J. Phys. Chem. Lett.* **2014**, *5*, 4319.
[54] B. Marchand, P. Jalkanen, V. Tuboltsev, M. Vehkamäki, M. Puttaswamy, M. Kemell, K. Mizohata, T. Hatanpää, A. Savin, J. Räisänen, M. Ritala, M. Leskelä, *J. Phys. Chem. C* **2016**, *120*, 7313.
[55] Y. T. Chong, E. M. Y. Yau, K. Nielsch, J. Bachmann, *Chem. Mater.* **2010**, *22*, 6506.
[56] C. D. Pham, J. Chang, M. A. Zurbuchen, J. P. Chang, *ACS Appl. Mater. Interfaces* **2017**, *9*, 36980.
[57] S. E. Shirsath, X. Liu, Y. Yasukawa, S. Li, A. Morisako, *Sci. Rep.* **2016**, *6*, 30074.
[58] S. E. Shirsath, D. Wang, J. Zhang, A. Morisako, S. Li, X. Liu, *ACS Appl. Electron. Mater.* **2020**, *2*, 3650.

[59] A. C. Marques, J. Faria, P. Perdigão, B. M. M. Faustino, R. Ritasalo, K. Costabello, R. C. da Silva, I. Ferreira, *Sci. Rep.* **2019**, *9*, 17919.
[60] S. Li, C. Q. Sun, H. S. Park, *Thin Solid Films* **2006**, *504*, 108.
[61] C. A. Wilson, R. K. Grubbs, S. M. George, *Chem. Mater.* **2005**, *17*, 5625.
[62] A. Ceballos, Z. Chen, O. Schneider, C. Bordel, L.-W. Wang, F. Hellman, *Appl. Phys. Lett.* **2017**, *111*, 172401.
[63] C. Q. Yu, H. Li, Y. M. Luo, L. Y. Zhu, Z. H. Qian, T. J. Zhou, *Phys. Lett. A* **2019**, *383*, 2424.